

Technical Note

Fast quantitative susceptibility mapping using 3D EPI and total generalized variation



Christian Langkammer^{a,b,*}, Kristian Bredies^c, Benedikt A. Poser^d, Markus Barth^e, Gernot Reishofer^f, Audrey Peiwen Fan^{g,h}, Berkin Bilgic^a, Franz Fazekas^b, Caterina Mainero^a, Stefan Ropele^b

^a MGH Athinoula A. Martinos Center for Biomedical Imaging, Department of Radiology, Harvard Medical School, Boston, MA, USA

^b Department of Neurology, Medical University of Graz, Graz, Austria

^c Institute of Mathematics and Scientific Computing, University of Graz, Graz, Austria

^d Faculty of Psychology and Neuroscience, Maastricht University, Maastricht, The Netherlands

^e Centre for Advanced Imaging, The University of Queensland, Brisbane, Australia

^f Department of Radiology, Division of Neuroradiology, Medical University of Graz, Graz, Austria

^g Department of Electrical Engineering and Computer Science, Massachusetts Institute of Technology, Cambridge, MA, USA

^h Lucas Center for Imaging, Stanford University, Stanford, CA, USA

ARTICLE INFO

Article history:

Accepted 20 February 2015

Available online 27 February 2015

Keywords:

Quantitative susceptibility mapping

Total generalized variation

Total variation

Dipole inversion

Iron

Myelin

Susceptibility tensor imaging

ABSTRACT

Quantitative susceptibility mapping (QSM) allows new insights into tissue composition and organization by assessing its magnetic property. Previous QSM studies have already demonstrated that magnetic susceptibility is highly sensitive to myelin density and fiber orientation as well as to para- and diamagnetic trace elements. Image resolution in QSM with current approaches is limited by the long acquisition time of 3D scans and the need for high signal to noise ratio (SNR) to solve the dipole inversion problem.

We here propose a new total-generalized-variation (TGV) based method for QSM reconstruction, which incorporates individual steps of phase unwrapping, background field removal and dipole inversion in a single iteration, thus yielding a robust solution to the reconstruction problem. This approach has beneficial characteristics for low SNR data, allowing for phase data to be rapidly acquired with a 3D echo planar imaging (EPI) sequence. The proposed method was evaluated with a numerical phantom and in vivo at 3 and 7 T.

Compared to total variation (TV), TGV–QSM enforced higher order smoothness which yielded solutions closer to the ground truth and prevented stair-casing artifacts. The acquisition time for images with 1 mm isotropic resolution and whole brain coverage was 10 s on a clinical 3 Tesla scanner.

In conclusion, 3D EPI acquisition combined with single-step TGV reconstruction yields reliable QSM images of the entire brain with 1 mm isotropic resolution in seconds. The short acquisition time combined with the robust reconstruction may enable new QSM applications in less compliant populations, clinical susceptibility tensor imaging, and functional resting state examinations.

© 2015 Elsevier Inc. All rights reserved.

Introduction

Quantitative susceptibility mapping (QSM) measures a fundamental physical property in vivo that is highly sensitive to tissue molecular composition and disease-induced tissue damage (De Rochefort et al., 2010; Marques and Bowtell, 2005; Shmueli et al., 2009). The clinical value of QSM has not yet been fully explored but holds great promise

for vascular, inflammatory and neurodegenerative diseases of the brain (Wang and Liu, 2014).

To date, QSM has been shown to differentiate micro-bleeds from calcifications which otherwise appear similar on T2*-weighted images (Kaaouana et al., 2014; Liu et al., 2011b; Schweser et al., 2010a). QSM allows better delineation of deep brain structures from adjacent tissue than T2*-weighted images (Deistung et al., 2013; Eskreis-winkler et al., 2013; Schäfer et al., 2012); can be used to assess myelin content and the extent of loss during demyelination (Argyridis et al., 2013; Stüber et al., 2014; Wharton and Bowtell, 2014); and has the potential to map oxygen saturation along venous vasculature (Fan et al., 2013). Due to the strong paramagnetic effect of iron, iron levels in gray matter can be measured accurately with QSM to enable more specific investigation of age-related and disease-induced iron deposition (Langkammer et al., 2012; Li et al., 2013; Sun et al., 2014). Iron accumulation has

Abbreviations: EPI, echo planar imaging; GRE, gradient recalled echo; QSM, quantitative susceptibility mapping; SHARP, sophisticated harmonic artifact reduction on phase data; TGV, total generalized variation; TV, total variation.

* Corresponding author at: MGH/HST Athinoula A. Martinos Center for Biomedical Imaging, 13th Street, Building 149, Charlestown, MA 02129, USA.

E-mail address: clangkammer@mgh.harvard.edu (C. Langkammer).

also been linked to the molecular cascade underlying neurodegeneration, which is in line with recent findings of increased susceptibility in deep gray matter of patients with Parkinson's and Alzheimer's diseases (Acosta-Cabronero et al., 2013; Langkammer et al., 2014; Lotfipour et al., 2012; Raven et al., 2013). In multiple sclerosis studies, QSM has utility to detect tissue demyelination changes in early stages of the disease (Blazejewska et al., 2014; Langkammer et al., 2013; Rudko et al., 2014) and to monitor susceptibility in multiple sclerosis lesions that may indicate iron accumulation or demyelination (Chen et al., 2014; Eskreis-Winkler et al., 2014; Wiggermann et al., 2013; Wisnieff et al., 2014).

Three dimensional (3D) GRE sequences for clinical QSM studies require acquisition times of at least 5 min when resolutions of $1 \times 1 \times 2 \text{ mm}^3$ or better are desired. A higher resolution comes at the cost of prolonged acquisition times, reduced SNR and a higher sensitivity to patient-induced motion artifacts. When performing QSM, artifacts may also arise from physiological fluctuations, motion and blood flow. Additionally, modulation of oxygenation levels and organ motion during respiration may affect QSM results (Wen et al., 2014).

Several strategies have been described to address these problems. To reduce movement artifacts with shorter acquisition times, previous work has adopted 2D instead of 3D readout strategies. Fast 2D acquisitions with echo planar imaging (EPI) have been demonstrated for functional QSM at 9.4 T (Balla et al., 2014) and single-shot 2D EPI has shown promise for rapid assessment of QSM at clinical field strengths (Sun and Wilman, 2014). 2D imaging can yield comparable SNR efficiency to 3D acquisitions due to sequence considerations, particularly in low-resolution acquisitions. However, for high-resolution isotropic imaging, the SNR benefit from 3D imaging can be substantial. Instead of 2D scans, we here propose to acquire phase data with a 3D echo planar imaging sequence (Poser et al., 2010). The MR acquisition of 3D EPI images with 1 mm isotropic resolution and whole brain coverage requires approximately 10 s on a clinical 3 Tesla system. This efficient acquisition can be combined with a robust TGV-based QSM algorithm which reconstructs susceptibility maps in a single integrated step that includes background phase removal and dipole inversion.

In summary, the specific contributions of this work are:

- Combination of rapid 3D EPI acquisition and integrated QSM reconstruction.
- Incorporating phase unwrapping, background field removal, and dipole inversion into a single integrated step, thereby obviating the need for parameter selection in background filtering.
- Use of TGV instead of TV penalty to avoid stair-casing artifacts.
- Making the source code freely available for reproducibility of the presented results.

Methods

Total generalized variation

Dipole inversion methods using total variation (TV) penalty have been proposed to reconstruct the underlying magnetic susceptibility distribution from gradient echo phase data (Bilgic et al., 2012; Khabipova et al., 2014; Liu et al., 2011a; Schweser et al., 2012). However, TV only takes the first derivative of the susceptibility distribution into account and does not enforce higher-order smoothness, resulting in so called staircase artifacts for images that are not piecewise constant. As an alternative, the total generalized variation (TGV) penalty shares convenient properties of the TV functional, but also promotes higher-order smoothness and therefore leads to more accurate solutions (Bredies et al., 2010; Yanez et al., 2013). Past applications of TGV in MRI include parallel imaging, diffusion tensor imaging and PatLoc reconstruction (Knoll et al., 2012, 2013; Valkonen et al., 2013), in

particular the under-sampled reconstruction and denoising of MR images as shown in Fig. 1 (Knoll et al., 2011).

Because TGV is the semi-norm on a Banach space, reconstruction problems with TGV penalty can be solved with tools developed for convex optimization problems. The well-known TV semi-norm of an image, or in the present case the susceptibility distribution χ , is described as:

$$\text{TV}(\chi) = \|\nabla\chi\|_M$$

where ∇ denotes the gradient and $\|\cdot\|_M$ the Radon norm (a generalization of the L^1 -norm). The TGV functional (here defined as second order TGV^2) itself represents a minimization problem:

$$\text{TGV}_{\alpha_1, \alpha_0}^2(\chi) = \min_w \alpha_1 \|\nabla\chi - w\|_M + \alpha_0 \|\varepsilon w\|_M.$$

Minimization is performed over all vector fields w , where ε denotes the symmetrized derivative for vector fields resulting in second-order symmetric tensor fields, $\varepsilon w = \frac{1}{2}(\nabla w + \nabla w^T)$. For example, the symmetrized derivative ε for the 2 dimensional case is defined as:

$$w = \begin{pmatrix} w_1 \\ w_2 \end{pmatrix}, \quad \varepsilon w = \begin{pmatrix} \frac{\partial w_1}{\partial x} & \frac{1}{2} \left(\frac{\partial w_1}{\partial y} + \frac{\partial w_2}{\partial x} \right) \\ \frac{1}{2} \left(\frac{\partial w_1}{\partial y} + \frac{\partial w_2}{\partial x} \right) & \frac{\partial w_2}{\partial y} \end{pmatrix}.$$

Second-order TGV^2 inherently balances locally the first and the second derivative of a function, as determined by the ratio of the positive weights α_1 and α_0 . Note that the ratio of α_1 and α_0 has been experimentally shown to be ideal for MR images between 2:1 and 3:1 and therefore no additional parameter is introduced (Knoll et al., 2011). For all data presented in this work, the ratio of α_1 and α_0 was fixed to 3:1 and the reconstruction parameters for the 1 mm isotropic 3D EPI data were then empirically evaluated within a range of two orders of magnitude (α_0 from 0.0001 to 0.01). The visually obtained optimum value pair of $\alpha = (\alpha_1, \alpha_0) = (0.0015, 0.0005)$ was utilized in this work.

Integrative QSM reconstruction using TGV

As QSM reconstruction usually involves multiple steps, errors may propagate in each step, e.g. the error from the background phase removal directly impacts the result of the dipole inversion. Our approach instead acts directly on the wrapped phase data and incorporates the background field removal by introducing an auxiliary variable in the iterative regularization process for the dipole inversion. Furthermore, in comparison to other methods such as SHARP (Schweser et al., 2010b), no threshold parameter has to be defined for background field removal.

QSM maps were recovered from the wrapped phase of single gradient echo data ϕ_{wrapped} . The recovery bases on an optimization procedure which operates on the Laplacian Δ of the unwrapped phase ϕ . The data $\Delta\phi$ can be obtained from $\Delta\phi_{\text{wrapped}}$, as described in (Schofield and Zhu, 2003), a technique which was first applied to QSM in (Li et al., 2011b; Schweser et al., 2013):

$$\Delta\phi = \text{Im} \left(\Delta e^{j\phi_{\text{wrapped}}} \cdot e^{-j\phi_{\text{wrapped}}} \right).$$

The dipole inversion is implemented directly on the Laplacian of the phase:

$$\frac{1}{3} \frac{\partial^2 \chi}{\partial x^2} + \frac{1}{3} \frac{\partial^2 \chi}{\partial y^2} - \frac{2}{3} \frac{\partial^2 \chi}{\partial z^2} = \frac{1}{2\pi T_E \gamma B_0} \Delta\phi \text{ for the susceptibility } \chi.$$

Here, the background field was implicitly incorporated by the introduction of an auxiliary variable ψ whose Laplacian is required to be equal to the discrepancy of this equation on the brain mask Ω . This auxiliary variable was penalized by a squared L^2 -norm, i.e., integrating its

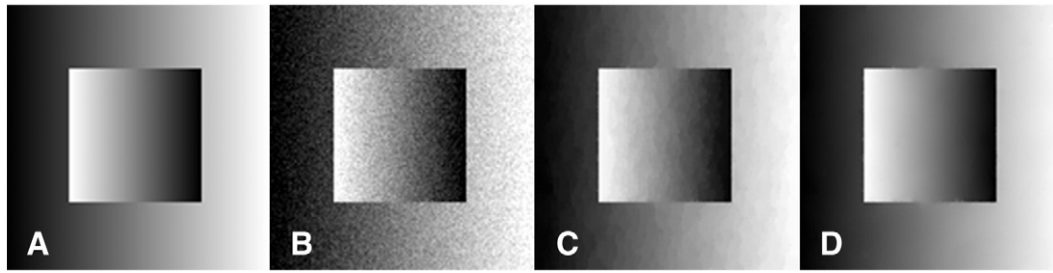


Fig. 1. Original image (A), noisy image (B) and results of TV- (C) and TGV-based (D) variational denoising.

squared absolute value over Ω while the brain mask was obtained by using the Brain Extraction Tool from FSL (Smith et al., 2004). Additionally, the inversion was regularized with TGV of second order and regularization parameters $\alpha = (\alpha_0, \alpha_1)$, which in particular realize a weighting, resulting in the variational problem:

$$\min_{\chi, \psi} \int |\psi|^2 dx + \text{TGV}_\alpha^2(\chi) \text{ subject to } \Delta\psi = \frac{1}{3} \frac{\partial^2 \chi}{\partial x^2} + \frac{1}{3} \frac{\partial^2 \chi}{\partial y^2} - \frac{2}{3} \frac{\partial^2 \chi}{\partial z^2} - \frac{1}{2\pi T_E \gamma B_0} \Delta\phi \text{ in } \Omega.$$

The TGV functional itself introduces one more auxiliary variable as

$$\text{TGV}_\alpha^2(\chi) = \min_w \alpha_1 \|\nabla \chi - w\|_M + \alpha_0 \|\varepsilon w\|_M.$$

Where, again, ∇ and ε are the gradient and symmetrized derivative, respectively, and $\|\cdot\|_M$ denotes the Radon norm, see (Bredies et al., 2010) for details.

The solution of this optimization problem yields susceptibility maps in a single step – without the need of separate phase unwrapping and background field fitting. This is enabled by using only the Laplacian of the unwrapped phase ($\Delta\phi$) in the inversion problem; thus, the unwrapped phase ϕ is not recovered or used directly (Li et al., 2014; Zhou et al., 2014). Further, by the constraint on $\Delta\psi$, the discrepancy associated with the dipole inversion problem is realized by ψ . This discrepancy can be interpreted as the difference, in terms of the Laplacian, of χ convolved with the dipole kernel and the given phase ϕ . The minimization with respect to ψ thus corresponds to removal of the (harmonic) background field. Finally, minimization with respect to χ yields the TGV-regularized dipole inversion.

The optimization problem can be solved numerically by employing general primal–dual algorithms for finding saddle points for convex-concave problems. For the computations, the iterative method was implemented in Python as described in (Bredies, 2014; Chambolle and Pock, 2010) on a machine with two six-core AMD Opteron 2.2 GHz processors and 24 GB of RAM. The reconstruction time using the parameters described above and 1000 iteration steps was approximately 5 min for whole-brain data at 1 mm isotropic resolution.

The software developed for this TGV-based QSM reconstruction is freely available for academic purposes and can be obtained from: <http://www.neuroimaging.at/pages/research/quantitative-susceptibility-mapping.php>.

Simulated QSM reconstruction

A numerical phantom was adapted from the work of (Wisnieff et al., 2013) for the simulation of the QSM reconstruction based on TGV-regularization (Fig. 2A). Briefly, this phantom was created by automated segmentation of a brain into white matter, gray matter and cerebrospinal fluid (CSF). Susceptibilities were similar to values observed in vivo: CSF = 0 ppm, globus pallidus = 0.19 ppm, putamen = 0.09 ppm, thalamus = 0.07 ppm, red nucleus = 0.07 ppm, substantia nigra = 0.09 ppm, dentate nucleus = 0.09 ppm, caudate nucleus = 0.09 ppm, and cortical gray matter = 0.05 ppm. Based on the orientation of fiber bundles, susceptibilities of white matter structures range from -0.03

to -0.01 ppm. Geometric properties were derived from the imaging data (matrix size = $256 \times 256 \times 98$, resolution = $0.94 \times 0.94 \times 1.5$ mm³).

This phantom was extended with focal susceptibility perturbers mimicking air–tissue interfaces in the proximity of nasal and ear cavities. Additionally, two random focal susceptibility sources were placed outside the brain. Positions and magnitudes of these background field components were evaluated experimentally to obtain results similar to in vivo gradient echo phase images. Subsequently, the phantom was convolved with the dipole kernel using parameters to match the EPI acquisition (TE = 21 ms, 3 T) and wrapped to the interval $-\pi$ to π . Finally, white noise with maximum amplitude of 5% of this 2π interval was added. As final step the simulated phase data was masked by a brain mask only covering the brain parenchyma. Resulting phase images are presented in Fig. 2B.

In-vivo 3D EPI imaging

Three volunteers without known neurological disorder (age range = 24–32 years) underwent brain MRI at 3 T (TimTrio, Siemens Healthcare, Erlangen, Germany). Written informed consent was obtained from all subjects.

The MR protocol included a 3D gradient echo EPI sequence by (Poser et al., 2010) with 1 mm isotropic resolution (TR/TE = 69/21 ms, FOV = $230 \times 230 \times 176$ mm, FA = 17°, and 156 EPI partitions). Images were acquired using a 32 channel phased array coil with parallel under sampling of factor 4 and 6/8 partial Fourier applied along the primary phase encoding direction (ky). For each excitation 43 k-space lines were sampled which an echo spacing of 1.04 ms. Automated shimming was applied using the vendor's default implementation for EPI sequences. The acquisition for these parameters with whole brain coverage in 1 mm isotropic resolution took 10 s. Independently of the number of averages in the 3D EPI scan, approximately 17 s are needed once for the EPI reference and phase correction scans. Reconstruction was performed using the manufacturer's parallel imaging reconstruction algorithm, but with “Maxwell correction” disabled. The Maxwell correction accounts for Maxwell fields, the concomitant magnetic fields inherently generated by the gradient pulses before the EPI readout train, which consequently induce undesired phase variations in the complex images (Jezzard and Clare, 1999). In the present work this correction was disabled for the scans because the scanner vendor's correction method is applied for magnitude and phase images separately and would have led to improper phase values in the proximity of 2π phase wraps which subsequently cannot be unwrapped.

In total, 32 averages of the 3D EPI sequence were acquired resulting in a total acquisition time of 5 min 38 s. Data from the 32 measurements were saved individually for a subsequent analysis. The individual magnitude and phase images were combined into complex MR data and then averaged to obtain data from 1, 2, 3, ..., 31, and 32 virtual measurements. Subsequently, phase data derived from the complex MR data was used for QSM reconstruction while magnitude data was used for brain mask extraction.

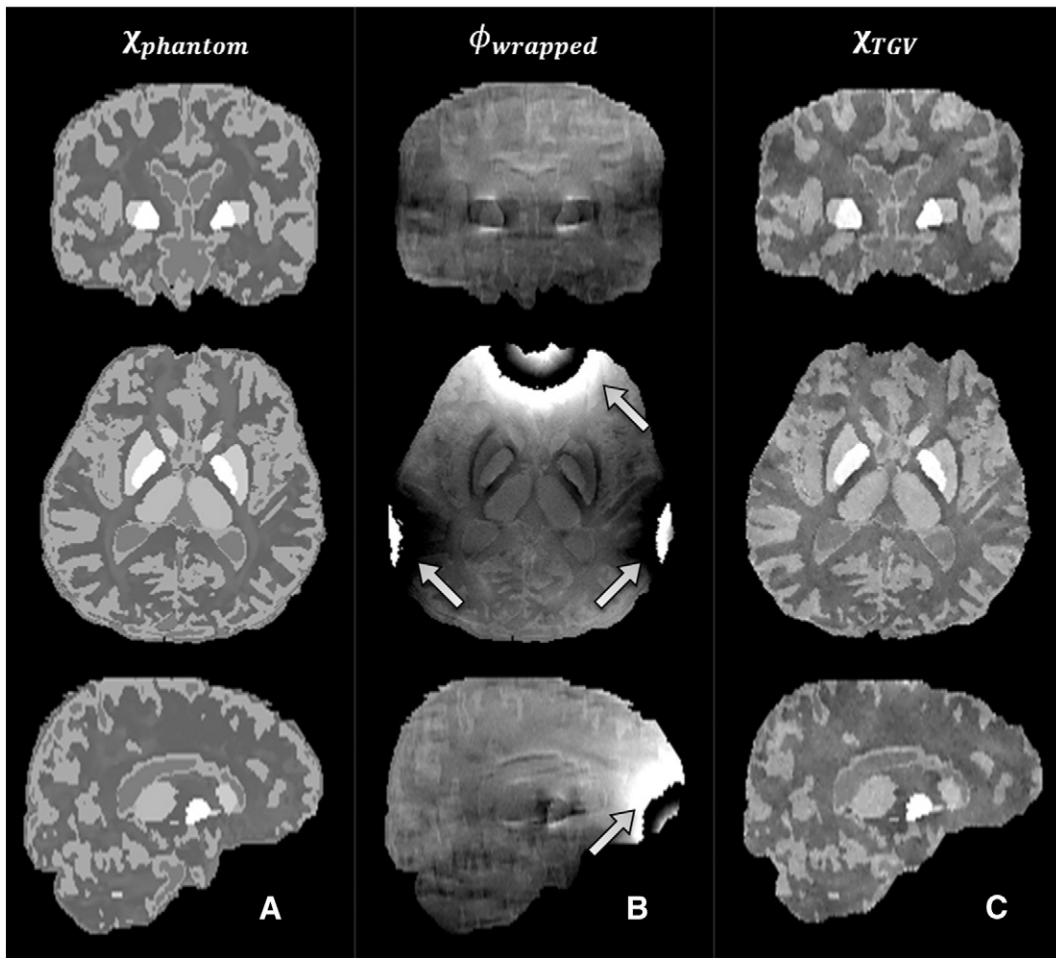


Fig. 2. Numerical susceptibility phantom (column A). Results of the forward simulation showing phase data after background perturbers mimicking air–tissue interfaces in the proximity of cavities (arrows) and noise have been added (B). Results of the QSM reconstruction using the TGV approach proposed in this work (C). Susceptibility maps $\chi_{phantom}$ and χ_{TGV} are scaled from -0.3 to 0.3 ppm, and phase images $\phi_{wrapped}$ from $-\pi$ to π .

Additionally, an MPRAGE sequence with 1 mm isotropic resolution (TR/TE/TI/FA = 1900 ms/2.19 ms/900 ms/9°) and a matrix size of $256 \times 256 \times 176$ was acquired with GRAPPA = 2 and an acquisition time of 3 min 29 s.

Regional QSM evaluation

Quantitative assessment of the proposed technique was performed in deep gray matter structures as these typically present with high iron levels relative to white matter structures. These brain structures, including the caudate nucleus, globus pallidus, and putamen, were segmented from the high resolution T1-weighted MPRAGE scan via FIRST, a segmentation and registration tool based on deformable models (Patenaude et al., 2011; Smith et al., 2004). The 3D masks obtained for these structures were eroded by at least 1 voxel and then were overlaid on the QSM images. To assess the impact of SNR, mean regional susceptibilities and standard deviations were calculated for each structure as a function of signal averages (ranging from 1 to 32 averages). Values from both hemispheres were averaged.

In vivo 3D GRE imaging

To demonstrate the TGV–QSM reconstruction on conventional high resolution gradient recalled echo (GRE) one healthy volunteer (age 32 years) underwent MR imaging at 7 T (Siemens Magnetom) with a 32 channel receive coil array. Imaging included a spoiled 3D GRE sequence (TE/TR = 15/25 ms, 0.5 mm isotropic resolution, BW =

100 Hz/px, matrix size = $384 \times 512 \times 240$) with Wave-CAIPI (Bilgic et al., 2014) using an acceleration factor of $R = 3 \times 3$ which resulted in a total acquisition time of 4 min 16 s. Wave-CAIPI traverses an efficient corkscrew k-space trajectory that spreads the aliasing evenly in 3D and fully exploits the variation in coil sensitivities to accelerate imaging with low artifact and noise amplification (maximum g-factor penalty $g_{max} = 1.14$).

Results

TGV–QSM of 3D EPI data

Results of the TGV-based single step QSM reconstruction are shown in Fig. 3. Visual inspection of the reconstruction demonstrated good contrast between cortical gray matter and subcortical white matter (Fig. 3A). In addition, the myelin-rich optical radiation was clearly visible. The deep gray matter nuclei were clearly delineated in all image planes and showed a strong intra-structural variation due to inhomogeneous iron distribution (Fig. 3A, B). Given that no additional priors were utilized for the QSM reconstruction, the absence of severe streaking artifacts is notable, which can be especially appreciated in the coronal view (Fig. 3C).

SNR analysis

TGV-based reconstruction yielded QSM images of good quality even from a single phase image without averaging. Not surprisingly,

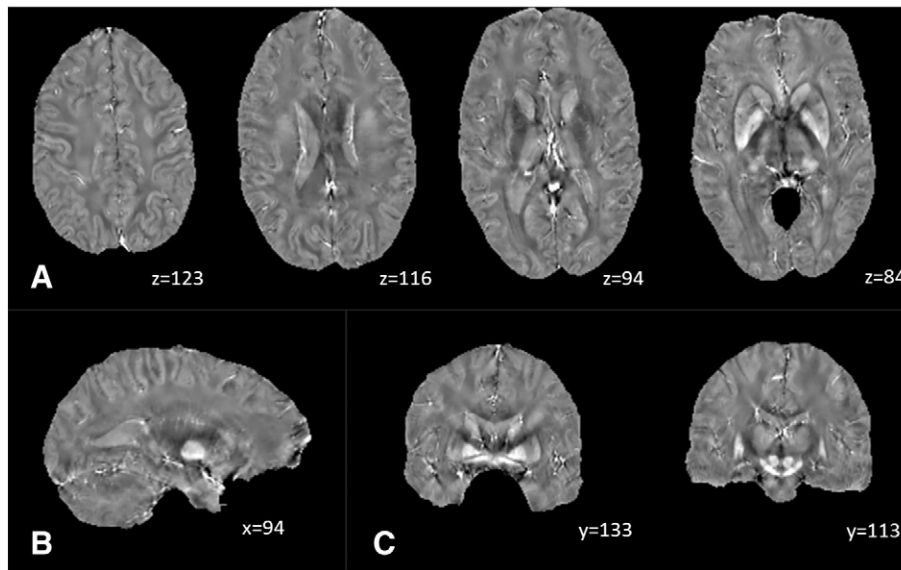


Fig. 3. Representative images of the QSM reconstruction with 32 averages by using TGV in transversal (A), sagittal (B) and coronal image planes (C). QSM images are scaled from -0.3 to 0.3 ppm. Note the good delineation of cortical structures (A) and deep gray matter nuclei (B and C).

more signal averages resulted in a more stable reconstruction and higher overall quality of the QSM images (Fig. 4).

Based on these individual reconstructions, the results of the ROI analysis are shown in Fig. 5. For four and more averages, the regional mean susceptibilities in the caudate, globus pallidus and putamen were largely independent of the number of signal averages. In all deep gray matter structures the variance in regional susceptibility constantly decreased with more averages acquired. However, acquiring more than 4 averages did not substantially change quantitative measurements and only marginally improved the SNR of the final susceptibility values.

TGV-QSM of GRE data

Fig. 6 shows the results of the TGV-QSM reconstruction from GRE data acquired with 0.5 mm isotropic resolution. Cortical gray matter yielded exquisite QSM contrast compared to adjacent white matter (Fig. 6 AB). Additionally, iron-loaded structures such as the putamen, globus pallidus, substantia nigra, and nucleus ruber can be delineated well from the adjacent tissue (Fig. 6 CD).

The level of streaking artifacts observed on the QSM maps is notably low although the GRE data has been obtained only from a single

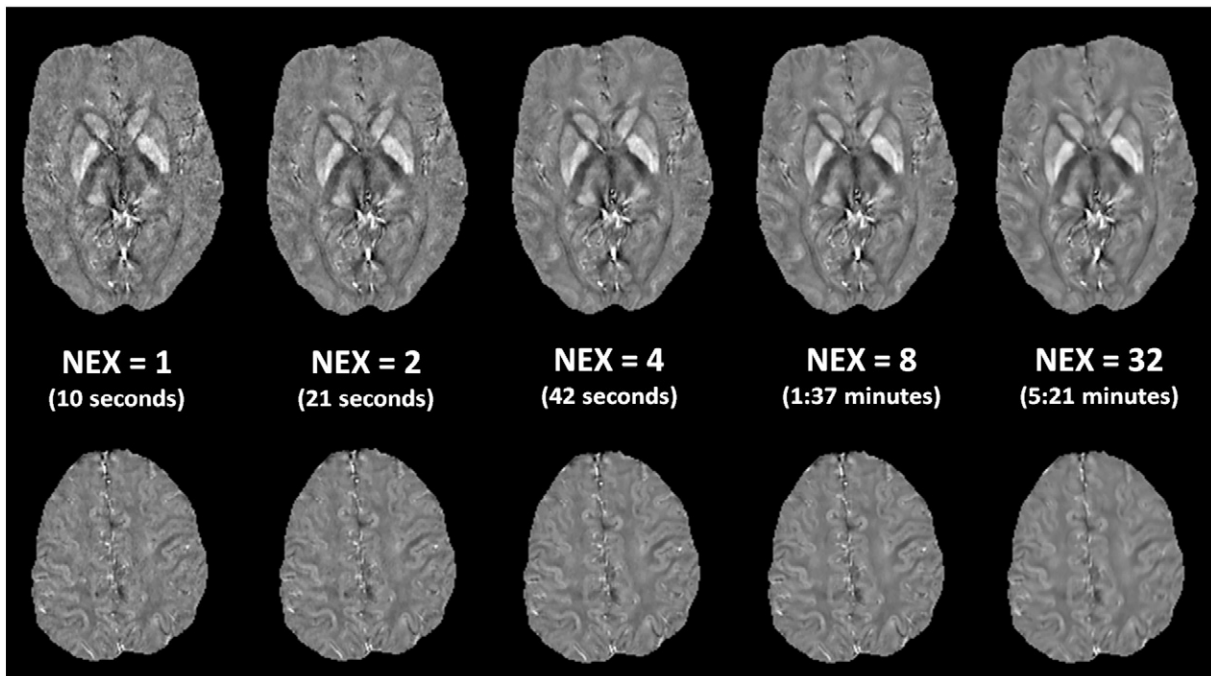


Fig. 4. Reconstructed QSM images with varying number of signal averages (NEX) and their respective acquisition times (not including a single EPI reference scan of 17 s). QSM images are scaled from -0.3 to 0.3 ppm. The upper row shows a representative slice of deep gray matter nuclei while the lower row demonstrates white-gray matter delineation of cortical structures.

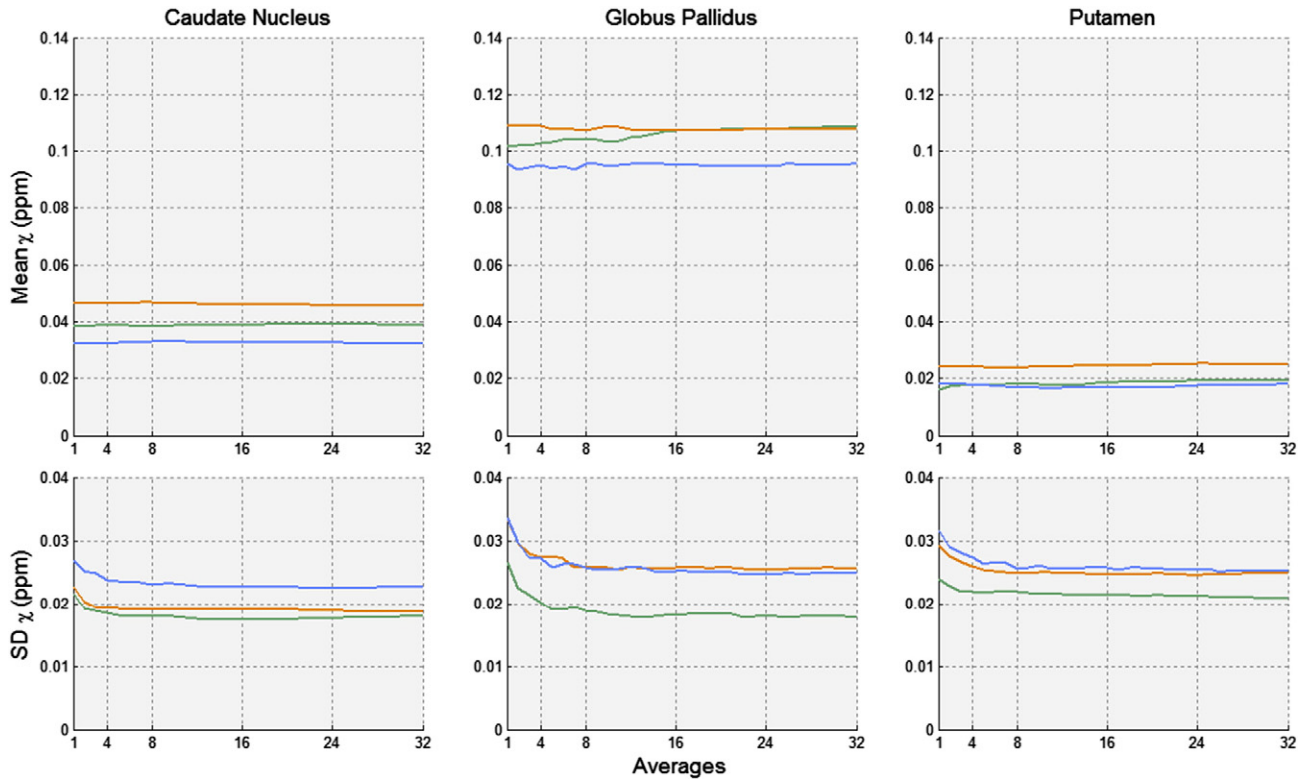


Fig. 5. Regional susceptibility plotted against the number of signal averages. Values represent mean susceptibility (upper row) and standard deviation (lower row, SD) of all voxels within a specific anatomical structure. Each color represents a single subject (age range 24–31 years).

orientation. The absence of severe artifacts can be observed best in coronal and sagittal views (Fig. 6 DE).

TV versus TGV based QSM reconstruction

The simulated phantom utilized in this work has been modified by an additional susceptibility gradient in the thalamus. The susceptibility gradient χ_{AP} is ranging from 0.20 to -0.20 ppm (anterior to posterior). Fig. 7 visualizes the differences of TV and TGV based QSM reconstruction where TV based QSM exhibited stair-casing artifacts which were not detectable when using TGV.

Discussion

The proposed TGV-QSM reconstruction is carried out in a single integrated optimization step which is algorithmically robust with respect to low SNR. Phase data from a single 3D EPI acquisition were acquired in

10 s with 1 mm isotropic resolution and yielded reasonable QSM images with moderate noise. Moreover, QSM images acquired in less than 1 min (4 signal averages plus EPI preparation) did not exhibit quantitative differences of susceptibility values in the deep gray matter structures compared to longer sampling.

The proposed algorithm combines phase unwrapping, background phase removal and dipole inversion as a single integrative step. Previous approaches separated these processes, such that errors from background field estimation might be propagated to the dipole inversion process. In addition, the presented reconstruction only requires a single parameter (α) whereas other QSM methods require both a regularization parameter and a SHARP threshold.

TGV is an extension of TV-based solutions which recover susceptibility shifts, e.g. between white and gray matter structures, while mitigating stair-casing artifacts which might be observed in white matter or in heterogeneous susceptibility distributions within gray matter nuclei. This improvement is especially important when no additional priors

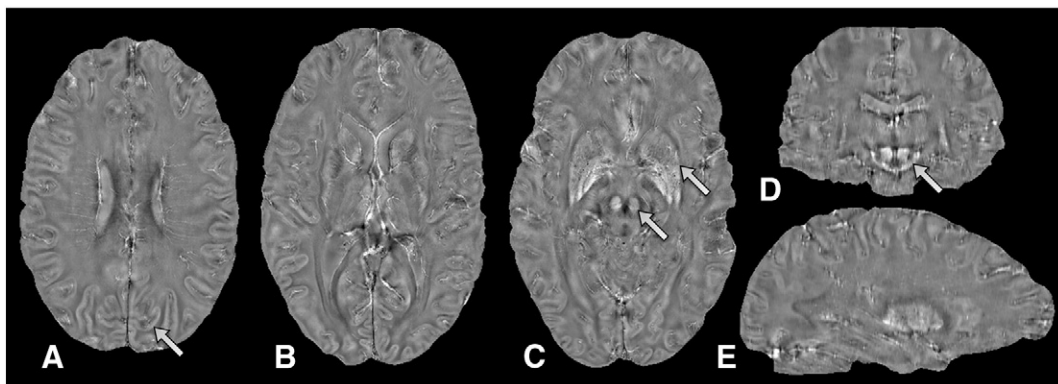


Fig. 6. Results of the TGV-QSM reconstructions obtained by a conventional GRE sequence (0.5 mm isotropic resolution). Images are scaled from -0.25 to 0.25 ppm.

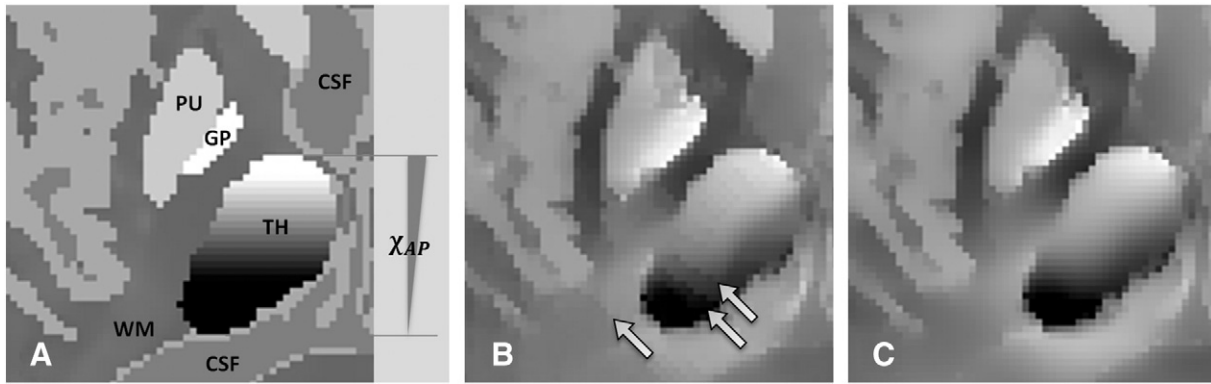


Fig. 7. Numerical susceptibility phantom (A) where the susceptibility in the thalamus (TH) has been modified to mimic a heterogeneous susceptibility distribution. While TV based QSM reconstruction yields stair-casing artifacts (B; arrows), the incorporation of higher order terms in the TGV based reconstruction yields smoother results within the nuclei but still preserves structural borders (C).

such as magnitude image gradients are incorporated in the reconstruction process or when investigating subtle changes, as observed in multiple sclerosis lesions relative to adjacent normal appearing white matter. TGV-based QSM reconstruction provides more accurate solutions than TV by suppressing stair-casing artifacts of the inversion problem because higher-order information is incorporated in the reconstruction procedure. However, assessing the differences of TV and TGV regularized QSM is challenging for in vivo data due to the lack of a known ground truth. To circumvent this issue we utilized a simulated phantom. Fig. 7 shows that TV based QSM exhibited stair-casing artifacts which were not detectable when using TGV.

Using EPI readout strategies for QSM is a relatively novel concept. Recently published work showed that 2D EPI acquisition is faster and more efficient in SNR than conventional GRE acquisitions. Consequently, it was proposed for functional QSM which aims to quantitatively assess BOLD changes (Balla et al., 2014). Another recent study elegantly demonstrated the feasibility of using 2D EPI for acquiring QSM within a few seconds (Sun and Wilman, 2014). However, due to its data sampling scheme, EPI is more sensitive to gradient performance, chemical shift effects, and bias field than conventional GRE. Although these effects might influence the gradient echo phase and the QSM reconstruction, recent work has shown that 2D EPI acquisition yields close to identical susceptibilities to standard GRE acquisition with a very high correlation ($r^2 = 0.96$). Fig. 6 shows images of the TGV-QSM reconstruction from data acquired by a GRE sequence where the GRE revealed more subtle anatomical details relative to EPI because of better spatial resolution. However, the susceptibilities obtained from the GRE were not quantitatively compared to the 3D EPI acquisition as different voxel sizes were used (Deistung et al., 2008; Haacke et al., 2014). TGV-QSM demonstrated a low level of streaking artifacts for the 3D EPI data, but also for the GRE data shown in this paper (observable in the coronal views in Figs. 3 and 6).

Beside QSM, EPI acquisition has been used for susceptibility weighted imaging (SWI) and T2* weighted imaging (Sati et al., 2012, 2014; Xu and Haacke, 2008; Zwanenburg et al., 2011). Compared to single shot methods, segmented EPI can achieve higher spatial resolutions and a lower level of geometrical distortions which come at the cost of increased scan time. In the present work we utilized 3D EPI which is, in most applications, more efficient than 2D with respect to SNR and allows thinner slices with better slice profiles to be acquired in reasonable acquisition times (Poser et al., 2010). However, application of physiological noise correction has demonstrated higher sensitivity for 3D than 2D acquisition in functional MRI studies (Lutti et al., 2013). Additionally, 3D EPI is readily available as sequence package for all major MRI system vendors and its conventional readout minimizes the need for more complex reconstruction from non-Cartesian trajectories.

Nevertheless, the speed-up of 3D EPI compared to GRE acquisition comes at the price of increased susceptibility artifacts which are present

in cortical regions in the proximity of sinuses and cavities. Fortunately, EPI based readouts are widely utilized in functional MRI and algorithms to correct these distortions have been proposed. An elegant method is to reverse the phase encoding direction (Andersson et al., 2003; Chang and Fitzpatrick, 1992), such that half of the acquisition is done in AP direction and half in PA direction. In this manner, the susceptibility-induced off-resonance field can be estimated and a corrected image can be calculated. This technique is amenable to our setup (e.g. two averages each per phase-encoding direction), and can be implemented in post-processing without additional scan time cost. Nevertheless, because of different sensitivity for susceptibility artifacts and different preprocessing steps such as geometrical distortion correction, we here did not focus on a side-by-side comparison between QSM reconstructions from GRE and EPI data with the proposed QSM approach. Instead, we demonstrated the applicability of TGV-QSM for different sequences with an emphasis on low SNR data from EPI and highly accelerated GRE acquisitions.

This work has its limitations. At the first glance, TGV of second order has two regularization parameters (α_0 and α_1) and therefore seems to introduce an additional regularization parameter compared to TV. Previous work assessing TGV² for medical image processing has demonstrated that the weights balancing the first to the second order terms are ideal between 2:1 and 3:1 (Knoll et al., 2011). Therefore, in this work the ratio of α_0 to α_1 was fixed and, thus, no additional parameter has to be considered. We did not investigate the selection of the regularization parameter set systematically as the present work focused on the impact of SNR and the required measurement time in a clinical setup. Both the 3D EPI data as well as the GRE data shown in this paper were reconstructed with the same regularization parameter set α . Although the voxel volume of those two sequences differs by a factor of 8, the resulting images show reasonable susceptibility contrast with a high level of details in particular in the cortex. However, the 7 T data might be over-regularized in central regions, which is subject to further investigations. This highlights the need for fine-tuning the regularization parameter set α for different sequence parameters under consideration of the subjective visual preference. This intrinsic difficulty of regularized QSM approaches was demonstrated and discussed in a recent review paper comparing various different algorithms for QSM (Wang and Liu, 2014).

For the SNR analysis, we emulated the situation of a clinical study where deep gray matter structures are investigated by region of interest analysis (Langkammer et al., 2013). These structures contain high levels of iron and thus QSM can be used to compare a patient cohort to controls or to longitudinally monitor disease progression. In this work, we did not include white matter regions due to its relatively low susceptibility values and because consideration of anisotropic susceptibility due to the white matter fiber orientation requires multi-orientation (head-tilting) measurements (Denk et al., 2011; Li et al., 2011a; Li and van Zijl, 2014).

In conclusion, QSM with 1 mm isotropic resolution in 10 s was demonstrated by combining phase imaging with 3D EPI and an integrated single step QSM reconstruction with TGV. Promising applications include multi-orientation QSM and susceptibility tensor imaging, where typical scan times currently are still longer than 1 h (Liu, 2010; Liu et al., 2009). Imaging of less-compliant patients and the retrospective assessment of the BOLD response in resting state functional MRI may also benefit from the fast acquisition and robust QSM reconstruction of the new approach.

Acknowledgments

We are grateful to Pınar Senay Özbay and Daniel Brenner for their help and for valuable feedback on the algorithm. This work was supported by the Austrian Science Fund (FWF project P23576 and FWF special research program SFB F32 “Mathematical Optimization and Applications in Biomedical Sciences”), BioTechMed Graz and NAWI Graz.

References

- Acosta-Cabrero, J., Williams, G.B., Cardenas-Blanco, A., Arnold, R.J., Lupson, V., Nestor, P.J., 2013. In vivo quantitative susceptibility mapping (QSM) in Alzheimer's disease. *PLoS One* 8, e81093. <http://dx.doi.org/10.1371/journal.pone.0081093>.
- Andersson, J.L.R., Skare, S., Ashburner, J., 2003. How to correct susceptibility distortions in spin-echo echo-planar images: application to diffusion tensor imaging. *Neuroimage* 20, 870–888. [http://dx.doi.org/10.1016/S1053-8119\(03\)00336-7](http://dx.doi.org/10.1016/S1053-8119(03)00336-7).
- Argyridis, I., Li, W., Johnson, G.A., Liu, C., 2013. Quantitative magnetic susceptibility of the developing mouse brain reveals microstructural changes in the white matter. *Neuroimage* 88C, 134–142. <http://dx.doi.org/10.1016/j.neuroimage.2013.11.026>.
- Balla, D.Z., Sanchez-Panchuelo, R.M., Wharton, S.J., Hagberg, G.E., Scheffler, K., Francis, S.T., Bowtell, R., 2014. Functional quantitative susceptibility mapping (fQSM). *Neuroimage* 100, 112–124.
- Bilgic, B., Pfefferbaum, A., Rohlfing, T., Sullivan, E.V., Adalsteinsson, E., 2012. MRI estimates of brain iron concentration in normal aging using quantitative susceptibility mapping. *Neuroimage* 59, 2625–2635. <http://dx.doi.org/10.1016/j.neuroimage.2011.08.077>.
- Bilgic, B., Gagoski, B.A., Cauley, S.F., Fan, A.P., Polimeni, J.R., Grant, P.E., Wald, L.L., Setsompop, K., 2014. Wave-CAIPI for highly accelerated 3D imaging. *Magn. Reson. Med.* 00, 1–11. <http://dx.doi.org/10.1002/mrm.25347>.
- Blazewjaska, A.I., Al-Radaideh, A.M., Wharton, S., Lim, S.Y., Bowtell, R.W., Constantinescu, C.S., Gowland, P.A., 2014. Increase in the iron content of the substantia nigra and red nucleus in multiple sclerosis and clinically isolated syndrome: a 7 Tesla MRI study. *J. Magn. Reson. Imaging* <http://dx.doi.org/10.1002/jmri.24644>.
- Bredies, K., 2014. Recovering piecewise smooth multichannel images by minimization of convex functionals with total generalized variation penalty. *Efficient Algorithms for Global Optimization Methods in Computer Vision*. Springer, pp. 44–77.
- Bredies, K., Kunisch, K., Pock, T., 2010. Total generalized variation. *SIAM J. Imaging Sci.* 3, 492–526. <http://dx.doi.org/10.1137/090769521>.
- Chambolle, A., Pock, T., 2010. A first-order primal-dual algorithm for convex problems with applications to imaging. *J. Math. Imaging Vis.* 40, 120–145. <http://dx.doi.org/10.1007/s10851-010-0251-1>.
- Chang, H., Fitzpatrick, J.M., 1992. A technique for accurate magnetic resonance imaging in the presence of field inhomogeneities. *IEEE Trans. Med. Imaging* 11, 319–329. <http://dx.doi.org/10.1109/42.158935>.
- Chen, W., Gauthier, S.A., Gupta, A., Comunale, J., Liu, T., Wang, S., Pei, M., Pitt, D., Wang, Y., 2014. Quantitative susceptibility mapping of multiple sclerosis lesions at various ages. *Radiology* 271, 183–192. <http://dx.doi.org/10.1148/radiol.13130353>.
- De Rochefort, L., Liu, T., Kressler, B., Liu, J., Spincemaille, P., Lebon, V., Wu, J., Wang, Y., 2010. Quantitative susceptibility map reconstruction from MR phase data using Bayesian regularization: validation and application to brain imaging. *Magn. Reson. Med.* 63, 194–206. <http://dx.doi.org/10.1002/mrm.22187>.
- Deistung, A., Rauscher, A., Sedlacik, J., Stadler, J., Witoszynski, S., Reichenbach, J.R., 2008. Susceptibility weighted imaging at ultra high magnetic field strengths: theoretical considerations and experimental results. *Magn. Reson. Med.* 60, 1155–1168. <http://dx.doi.org/10.1002/mrm.21754>.
- Deistung, A., Schäfer, A., Schweser, F., Biedermann, U., Turner, R., Reichenbach, J.R., 2013. Toward in vivo histology: a comparison of quantitative susceptibility mapping (QSM) with magnitude-, phase-, and R2*-imaging at ultra-high magnetic field strength. *Neuroimage* 65, 299–314. <http://dx.doi.org/10.1016/j.neuroimage.2012.09.055>.
- Denk, C., Hernandez Torres, E., MacKay, A., Rauscher, A., 2011. The influence of white matter fibre orientation on MR signal phase and decay. *NMR Biomed.* 24, 246–252. <http://dx.doi.org/10.1002/nbm.1581>.
- Eskreis-winkler, S., Schweitzer, A.D., Liu, T., Chen, W., Kaplitt, M.G., Tsiouris, A.J., Wang, Y., 2013. Improved subthalamic nucleus depiction with quantitative susceptibility mapping. *Radiology* 269, 216–223. <http://dx.doi.org/10.1148/radiol.13121991>.
- Eskreis-Winkler, S., Deh, K., Gupta, A., Liu, T., Wisniewski, C., Jin, M., Gauthier, S. a., Wang, Y., Spincemaille, P., 2014. Multiple sclerosis lesion geometry in quantitative susceptibility mapping (QSM) and phase imaging. *J. Magn. Reson. Imaging* 00, 1–6. <http://dx.doi.org/10.1002/jmri.24745>.
- Fan, A.P., Bilgic, B., Gagnon, L., Witzel, T., Bhat, H., Rosen, B.R., Adalsteinsson, E., 2013. Quantitative oxygenation venography from MRI phase. *Magn. Reson. Med.* 00, 1–11. <http://dx.doi.org/10.1002/mrm.24918>.
- Haacke, E.M., Liu, S., Buch, S., Zheng, W., Wu, D., Ye, Y., 2014. Quantitative susceptibility mapping: current status and future directions. *Magn. Reson. Imaging* 33, 1–25. <http://dx.doi.org/10.1016/j.mri.2014.09.004>.
- Jezzard, P., Clare, S., 1999. Sources of distortion in functional MRI data. *Hum. Brain Mapp.* 8, 80–85.
- Kaouana, T., de Rochefort, L., Samaille, T., Thiery, N., Dufouil, C., Delmaire, C., Dormont, D., Chupin, M., 2014. 2D harmonic filtering of MR phase images in multicenter clinical setting: toward a magnetic signature of cerebral microbleeds. *Neuroimage* 104, 287–300. <http://dx.doi.org/10.1016/j.neuroimage.2014.08.024>.
- Khabipova, D., Wiaux, Y., Gruetter, R., Marques, J.P., 2014. A modulated closed form solution for quantitative susceptibility mapping – a thorough evaluation and comparison to iterative methods based on edge prior knowledge. *Neuroimage* 107, 163–174. <http://dx.doi.org/10.1016/j.neuroimage.2014.11.038>.
- Knoll, F., Bredies, K., Pock, T., Stollberger, R., 2011. Second order total generalized variation (TGV) for MRI. *Magn. Reson. Med.* 65, 480–491. <http://dx.doi.org/10.1002/mrm.22595>.
- Knoll, F., Clason, C., Bredies, K., Uecker, M., Stollberger, R., 2012. Parallel imaging with non-linear reconstruction using variational penalties. *Magn. Reson. Med.* 67, 34–41. <http://dx.doi.org/10.1002/mrm.22964>.
- Knoll, F., Schultz, G., Bredies, K., Gallichan, D., Zaitsev, M., Hennig, J., Stollberger, R., 2013. Reconstruction of undersampled radial PatLoc imaging using total generalized variation. *Magn. Reson. Med.* 70, 40–52. <http://dx.doi.org/10.1002/mrm.24426>.
- Langkammer, C., Schweser, F., Krebs, N., Deistung, A., Goessler, A., Goessler, E., Sommer, K., Reishofer, G., Yen, K., Fazekas, F., Ropele, S., Reichenbach, J.R., 2012. Quantitative susceptibility mapping (QSM) as a means to measure brain iron? A post mortem validation study. *Neuroimage* 62, 1593–1599. <http://dx.doi.org/10.1016/j.neuroimage.2012.05.049>.
- Langkammer, C., Liu, T., Khalil, M., Enzinger, C., Jehna, M., Fuchs, S., Fazekas, F., Wang, Y., Ropele, S., 2013. Quantitative susceptibility mapping in multiple sclerosis. *Radiology* 267, 551–559. <http://dx.doi.org/10.1148/radiol.12120707>.
- Langkammer, C., Ropele, S., Pirpamer, L., Fazekas, F., Schmidt, R., 2014. MRI for iron mapping in Alzheimer's disease. *Neurodegener. Dis.* 13, 189–191. <http://dx.doi.org/10.1159/000353756>.
- Li, X., van Zijl, P.C.M., 2014. Mean magnetic susceptibility regularized susceptibility tensor imaging (MMSR-STI) for estimating orientations of white matter fibers in human brain. *Magn. Reson. Med.* 72, 610–619. <http://dx.doi.org/10.1002/mrm.25322>.
- Li, W., Wu, B., Avram, A.V., Liu, C., 2011a. Magnetic susceptibility anisotropy of human brain in vivo and its molecular underpinnings. *Neuroimage* 59, 2088–2097. <http://dx.doi.org/10.1016/j.neuroimage.2011.10.038>.
- Li, W., Wu, B., Liu, C., 2011b. Quantitative susceptibility mapping of human brain reflects spatial variation in tissue composition. *Neuroimage* 55, 1645–1656. <http://dx.doi.org/10.1016/j.neuroimage.2010.11.088>.
- Li, W., Wu, B., Batrachenko, A., Bancroft-Wu, V., Morey, R. a., Shashi, V., Langkammer, C., De Bellis, M.D., Ropele, S., Song, A.W., Liu, C., 2013. Differential developmental trajectories of magnetic susceptibility in human brain gray and white matter over the lifespan. *Hum. Brain Mapp.* 00, 2698–2713. <http://dx.doi.org/10.1002/hbm.22360>.
- Li, W., Avram, A.V., Wu, B., Xiao, X., Liu, C., 2014. Integrated Laplacian-based phase unwrapping and background phase removal for quantitative susceptibility mapping. *NMR Biomed.* 27, 219–227. <http://dx.doi.org/10.1002/nbm.3056>.
- Liu, C., 2010. Susceptibility tensor imaging. *Magn. Reson. Med.* 63, 1471–1477. <http://dx.doi.org/10.1002/mrm.22482>.
- Liu, T., Spincemaille, P., De Rochefort, L., Kressler, B., Wang, Y., 2009. Calculation of susceptibility through multiple orientation sampling (COSMOS): a method for conditioning the inverse problem from measured magnetic field map to susceptibility source image in MRI. *Magn. Reson. Med.* 61, 196–204. <http://dx.doi.org/10.1002/mrm.21828>.
- Liu, T., Liu, J., de Rochefort, L., Spincemaille, P., Khalidov, I., Ledoux, J.R., Wang, Y., 2011a. Morphology enabled dipole inversion (MED) from a single-angle acquisition: comparison with COSMOS in human brain imaging. *Magn. Reson. Med.* 66, 777–783. <http://dx.doi.org/10.1002/mrm.22816>.
- Liu, T., Surapaneni, K., Lou, M., Cheng, L., Spincemaille, P., Wang, Y., 2011b. Cerebral microbleeds: burden assessment by using quantitative susceptibility mapping. *Radiology* 262, 269–278. <http://dx.doi.org/10.1148/radiol.11110251>.
- Lotfipour, A.K., Wharton, S., Schwarz, S.T., Gontu, V., Schäfer, A., Peters, A.M., Bowtell, R.W., Auer, D.P., Gowland, P.A., Bajaj, N.P.S., 2012. High resolution magnetic susceptibility mapping of the substantia nigra in Parkinson's disease. *J. Magn. Reson. Imaging* 35. <http://dx.doi.org/10.1002/jmri.22752>.
- Lutti, A., Thomas, D.L., Hutton, C., Weiskopf, N., 2013. High-resolution functional MRI at 3 T: 3D/2D echo-planar imaging with optimized physiological noise correction. *Magn. Reson. Med.* 69, 1657–1664. <http://dx.doi.org/10.1002/mrm.24398>.
- Marques, J.P., Bowtell, R., 2005. Application of a Fourier-based method for rapid calculation of field inhomogeneity due to spatial variation of magnetic susceptibility. *Concepts Magn. Reson. Part B: Magn. Reson. Eng.* 25B, 65–78. <http://dx.doi.org/10.1002/cmr.b.20034>.
- Patenaude, B., Smith, S.M., Kennedy, D.N., Jenkinson, M., 2011. A Bayesian model of shape and appearance for subcortical brain segmentation. *Neuroimage* 56, 907–922.
- Poser, B. a., Koopmans, P.J., Witzel, T., Wald, L.L., Barth, M., 2010. Three dimensional echo-planar imaging at 7 Tesla. *Neuroimage* 51, 261–266. <http://dx.doi.org/10.1016/j.neuroimage.2010.01.108>.
- Raven, E.P., Lu, P.H., Tishler, T.A., Heydari, P., Bartzokis, G., 2013. Increased iron levels and decreased tissue integrity in hippocampus of Alzheimer's disease detected in vivo

- with magnetic resonance imaging. *J. Alzheimers Dis.* 37, 127–136. <http://dx.doi.org/10.3233/JAD-130209>.
- Rudko, D.A., Solovey, I., Gati, J.S., Kremenutzky, M., Menon, R.S., 2014. Multiple sclerosis: improved identification of disease-relevant changes in gray and white matter by using susceptibility-based MR imaging. *Radiology* 272, 851–864. <http://dx.doi.org/10.1148/radiol.14132475>.
- Sati, P., George, I.C., Shea, C.D., Gaitán, M.I., Reich, D.S., 2012. FLAIR*: a combined MR contrast technique for visualizing white matter lesions and parenchymal veins. *Radiology* 265, 926–932. <http://dx.doi.org/10.1148/radiol.12120208>.
- Sati, P., Thomasson, D., Li, N., Pham, D., Biassou, N., Reich, D., Butman, J., 2014. Rapid, high-resolution, whole-brain, susceptibility-based MRI of multiple sclerosis. *Mult. Scler.* 1–7. <http://dx.doi.org/10.1177/1352458514525868>.
- Schäfer, A., Forstmann, B.U., Neumann, J., Wharton, S., Mietke, A., Bowtell, R., Turner, R., 2012. Direct visualization of the subthalamic nucleus and its iron distribution using high-resolution susceptibility mapping. *Hum. Brain Mapp.* 33, 2831–2842. <http://dx.doi.org/10.1002/hbm.21404>.
- Schofield, M.A., Zhu, Y., 2003. Fast phase unwrapping algorithm for interferometric applications. *Opt. Lett.* 28, 1194–1196. <http://dx.doi.org/10.1364/OL.28.001194>.
- Schweser, F., Deistung, A., Lehr, B.W., Reichenbach, J.R., 2010a. Differentiation between diamagnetic and paramagnetic cerebral lesions based on magnetic susceptibility mapping. *Med. Phys.* 37, 5165–5178.
- Schweser, F., Deistung, A., Lehr, B.W., Reichenbach, J.R., 2010b. Quantitative imaging of intrinsic magnetic tissue properties using MRI signal phase: an approach to in vivo brain iron metabolism? *Neuroimage* 54, 2789–2807. <http://dx.doi.org/10.1016/j.neuroimage.2010.10.070>.
- Schweser, F., Sommer, K., Deistung, A., Reichenbach, J.R., 2012. Quantitative susceptibility mapping for investigating subtle susceptibility variations in the human brain. *Neuroimage* 62, 2083–2100. <http://dx.doi.org/10.1016/j.neuroimage.2012.05.067>.
- Schweser, F., Deistung, A., Sommer, K., Reichenbach, J.R., 2013. Toward online reconstruction of quantitative susceptibility maps: superfast dipole inversion. *Magn. Reson. Med.* 69, 1582–1594. <http://dx.doi.org/10.1002/mrm.24405>.
- Shmueli, K., de Zwart, J.A., van Gelderen, P., Li, T.-Q., Dodd, S.J., Duyn, J.H., 2009. Magnetic susceptibility mapping of brain tissue in vivo using MRI phase data. *Magn. Reson. Med.* 62, 1510–1522. <http://dx.doi.org/10.1002/mrm.22135>.
- Smith, S., Jenkinson, M., Woolrich, M., Beckmann, C., Behrens, T., Johansen-Berg, H., Bannister, P., De Luca, M., Drobnjak, I., Flitney, D., Niazy, R., Saunders, J., Vickers, J., Zhang, Y., De Stefano, N., Brady, J., Matthews, P., 2004. Advances in functional and structural MR image analysis and implementation as FSL. *Neuroimage* 23, 208–219.
- Stüber, C., Morawski, M., Schäfer, A., Labadie, C., Wähner, M., Leuze, C., Streicher, M., Barapatre, N., Reimann, K., Geyer, S., Spemann, D., Turner, R., 2014. Myelin and iron concentration in the human brain: a quantitative study of MRI contrast. *Neuroimage* <http://dx.doi.org/10.1016/j.neuroimage.2014.02.026>.
- Sun, H., Wilman, A.H., 2014. Quantitative susceptibility mapping using single-shot echo-planar imaging. *Magn. Reson. Med.* 00. <http://dx.doi.org/10.1002/mrm.25316> (n/a–n/a).
- Sun, H., Walsh, A.J., Lebel, R.M., Blevins, G., Catz, I., Lu, J.-Q., Johnson, E.S., Emery, D.J., Warren, K.G., Wilman, A.H., 2014. Validation of quantitative susceptibility mapping with Perls' iron staining for subcortical gray matter. *Neuroimage* 105, 486–492. <http://dx.doi.org/10.1016/j.neuroimage.2014.11.010>.
- Valkonen, T., Bredies, K., Knoll, F., 2013. Total generalized variation in diffusion tensor imaging. *SIAM J. Imaging Sci.* 6, 487–525. <http://dx.doi.org/10.1137/120867172>.
- Wang, Y., Liu, T., 2014. Quantitative susceptibility mapping (QSM): decoding MRI data for a tissue magnetic biomarker. *Magn. Reson. Med.* 00. <http://dx.doi.org/10.1002/mrm.25358> (n/a–n/a).
- Wen, J., Cross, A.H., Yablonskiy, D. a., 2014. On the role of physiological fluctuations in quantitative gradient echo MRI: implications for GEPCl, QSM, and SWI. *Magn. Reson. Med.* 00, 1–9. <http://dx.doi.org/10.1002/mrm.25114>.
- Wharton, S., Bowtell, R., 2014. Effects of white matter microstructure on phase and susceptibility maps. *Magn. Reson. Med.* 00, 1–12. <http://dx.doi.org/10.1002/mrm.25189>.
- Wiggermann, V., Hernández Torres, E., Vavasour, I.M., Moore, G.R.W., Laule, C., MacKay, A.L., Li, D.K.B., Traboulsee, A., Rauscher, A., 2013. Magnetic resonance frequency shifts during acute MS lesion formation. *Neurology* 81, 211–218. <http://dx.doi.org/10.1212/WNL.0b013e31829bfd63>.
- Wisnieff, C., Liu, T., Spincemaille, P., Wang, S., Zhou, D., Wang, Y., 2013. Magnetic susceptibility anisotropy: cylindrical symmetry from macroscopically ordered anisotropic molecules and accuracy of MRI measurements using few orientations. *Neuroimage* 70, 363–376. <http://dx.doi.org/10.1016/j.neuroimage.2012.12.050>.
- Wisnieff, C., Ramanan, S., Olesik, J., Gauthier, S., Wang, Y., Pitt, D., 2014. Quantitative susceptibility mapping (QSM) of white matter multiple sclerosis lesions: interpreting positive susceptibility and the presence of iron. *Magn. Reson. Med.* 00, 1–7. <http://dx.doi.org/10.1002/mrm.25420>.
- Xu, Y., Haacke, E.M., 2008. An iterative reconstruction technique for geometric distortion-corrected segmented echo-planar imaging. *Magn. Reson. Imaging* 26, 1406–1414. <http://dx.doi.org/10.1016/j.mri.2008.04.008>.
- Yanez, F., Fan, A., Bilgic, B., Milovic, C., Adalsteinsson, E., Irarrazaval, P., 2013. Quantitative susceptibility map reconstruction via a total generalized variation regularization. 2013 International Workshop on Pattern Recognition in Neuroimaging. IEEE, pp. 203–206 <http://dx.doi.org/10.1109/PRNI.2013.59>.
- Zhou, D., Liu, T., Spincemaille, P., Wang, Y., 2014. Background field removal by solving the Laplacian boundary value problem. *NMR Biomed.* <http://dx.doi.org/10.1002/nbm.3064>.
- Zwanenburg, J.J.M., Versluis, M.J., Luijten, P.R., Petridou, N., 2011. Fast high resolution whole brain T2* weighted imaging using echo planar imaging at 7 T. *Neuroimage* 56, 1902–1907. <http://dx.doi.org/10.1016/j.neuroimage.2011.03.046>.